Effect of Sides-spillage from Airframe on Scramjet Engine Performance *

Kouichiro TANI *1 , Takeshi KANDA *1, and Kenji KUDO *1
Daisuke AKIHISA *2

ABSTRACT

Pre-compression by the windward surface of the aerospace plane is necessary for scramjet operation. However, this pre-compression causes spillage from the high-pressure windward surface toward the sides of the plane. In order to examine the effects of this side-spillage, the performance of a scramjet engine was evaluated using a 1-D flow model, and payload to the low earth orbit estimated using an aerospace plane flight simulation. Prior to the simulation, tests with scramjet inlet models were conducted in a Mach 4 wind tunnel to identify the primary features of the side-spillage to assist in the simulation. The models were inclined from the flow direction to simulate the skewed flow near the side of the plane during side-spillage, and the experiments proved that the aerodynamic performance of the inlet was not affected by the inclination for the entrance Mach number given to the models. However, the mass capture ratio decreased due to reduction in the density of airflow as a result of the expansion. In the numerical estimate, side-spillage was modeled not to reduce the performance of the inlet, but to reduce mass flow to the inlet. The resulting decrease in airflow delivered to the engine due to spillage reduced thrust by 15%, while the corresponding payload decreased around 60%. Side fences were effective in preventing spillage.

Keywords: scramjet, inlet, spillage, aerospace plane, thrust, payload

概　　要

　スペースプレーン機体下面はスクラムジェットエンジン作動時の予圧縮に使われる。しかしこの予圧縮は、圧力の高くなった機体下面から側方への気流の漏れを生じる。この側方への漏れの効果を調べるために1次元モデルを使ってスクラムジェットのエンジン性能を計算し、またスペースプレーンの飛行シミュレーションによる低軌道へのペイロード計算を行った。シミュレーション計算に先立ち側方への漏れの概要を把握するために、マッハ4風洞においてスクラムジェットインレット模型の実験を行った。機体側方でのインレットに対し角度を持った空気が流入する状態を模擬するために、インレット模型は風洞気流に対し傾けた状態で設置した。実験の結果、気流の傾きはインレット性能には殆ど影響しないことがわかった。しかし機体側方への漏れ、それに伴う気流の密度減少のためにインレット流入空気流量は低下した。シミュレーション計算では、機体側方への気流の偏向によるインレット性能の低下は無いと仮定し、流入空気流量は機体側方からの膨脹波によって減少させた。その結果、側方からの漏れの影響でエンジン推力は15％減少し、ペイロードは60％減少した。側方からの漏れの防止にはサイドフェンスが有効である。

Nomenclatures

A	: cross section
D	: drag of the aerospace plane
F	: net propulsive force of the engine
F_{total}	: net thrust with drag on the windward surface of the airframe
g	: acceleration of gravity
h_r	: height of ramp of the inlet model
I_{sp}	: engine specific impulse
L	: lift of the aerospace plane
M	: Mach number
m	: mass of the aerospace plane
$\dot{m}$	: mass flow rate
P	: static pressure
P_t	: total pressure
P_w	: wall pressure
q	: dynamic pressure
R	: radius of the earth
t	: time
u	: velocity
x	: distance on the Earth surface
y	: coordinate normal to the top-wall in the inlet model
z	: lateral coordinate in the inlet model, height of aerospace plane
α	: ramp angle of the inlet model
δ	: inclination angle of the inlet model
γ	: inclination angle of the aerospace plane in the flight simulation
ρ	: density
θ	: angle between the engine thrust and the airframe velocity

Subscripts

a	: air
ex	: inlet exit
i	: inlet entrance
th	: inlet throat, i.e., end position of the convergent section of the inlet
∞	: flight condition
0	: estimated condition upstream of supposed expansion in front of inlets in inclination
1	: inlet model entrance
2	: inlet model exit

Introduction

Many configurations for the aerospace plane and engine have been proposed.[1)-4)] The common features of the various aerospace planes in terms of the engine mounting are as follows: (1) multiple engine modules mounted on the airframe, (2) side-by-side arrangement on the windward surface, and (3) pre-compression of the air by the windward airframe. Since the airframe width is finite, the pre-compression creates a gradient in pressure between the center and the sides of the airframe. The air spills out from the windward surface to the sides of the airframe. This is designated as 'sides-spillage' in the present study. The propagation of the expansion waves from the sides of the airframe affects the amount of airflow delivered to the engine. The flow condition with the sides-spillage is 3-D and very complicated. Therefore, in the present study, the flow field was simplified to a 2-D model. Figure 1 shows a schematic image of the sides-spillage. The 3-D flow field was projected to a 2-D plane (bottom view of Fig. 1). Due to the pressure gradient, there are a shock wave and an expansion fan from each corner of the airframe leading edge at each side of the airframe. Between the shock wave and the expansion fan, there is a slip line. The static pressures are the same across the slip line, as well as the flow directions. The area covered by the expansion fan is an affected region by the sides-spillage. The engine modules close to the sides of the airframe are in the
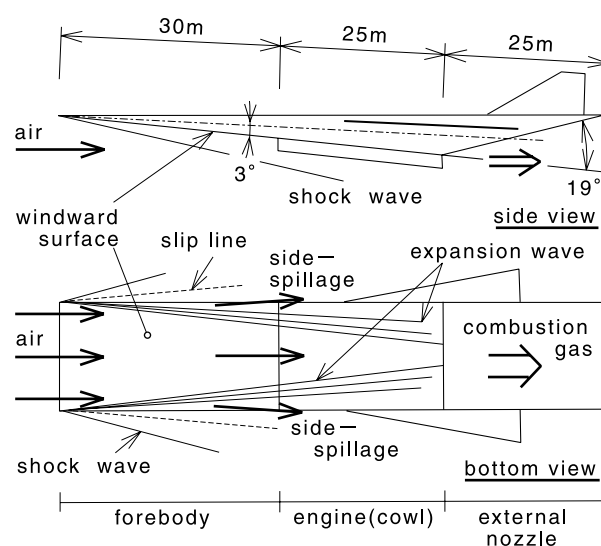

Fig. 1 Schematic diagram of the aerospace plane and the sides-spillage on the aerospace plane.

expansion waves, and the amount of airflow into the inlet decreases. Also, the inclination of the airflow may affect the engine and the inlet performances.

Inlets for scramjet engines have been studied at many laboratories, Institutes, Universities and the National Aerospace Laboratory of Japan. [5)-7)] The investigations were solely designed to clarify the characteristics of the inlet. However, no study was designed to clarify the effect of the inclined airflow on the inlet performance during the sides-spillage.

In the present study, the effects of the sides-spillage were investigated with mission simulations of the operation of the scramjet engine and the flight of the aerospace plane to the low earth orbit. Prior to the simulation, the effect of the inclination of the airflow due to the sides-spillage was investigated with preliminary experiments, and the primary effects on the inlet performance were adopted in the numerical simulations. Several options to prevent the sides-spillage were also discussed.

Numerical Simulation Methods

The impact of the sides-spillage on the engine performance and the payload was evaluated with simulations. A schematic diagram of the airframe for the prediction of the scramjet engine performance is shown in Fig. 1. The airframe had a wedge-shape, 2-D nose, and a body width of 15 m. The scramjet engine was on the windward ramp surface of the airframe. The engine was designed at the condition of the flight Mach number of 12. This design conditions followed the previous investigation,[8)] which showed that the operation of the scramjet engine up to Mach 12 resulted in the maximum payload. The angle of attack was 3°, and the windward surface angle from the airframe center axis was also 3°. In the simulation of the sides-spillage, both pressure and flow direction in the expanded flow coincided with those after the shock wave at the side of the airframe (Fig. 1). This condition was calculated with the 2-D shock wave relations and the Prandtl-Meyer function.

The height of the scramjet engine was 2 m at the entrance. With this configuration, the inlet was in the shock-on-lip condition at Mach 12. A width of the scramjet of 15 m was the same as that of the airframe. The overall contraction ratio of the engine was 5. Hydrogen fuel was injected normally into the combustor.

In the combustion tests with sub-scale scramjet engine models, sufficient combustion conditions were attained with normal fuel injection.[9),10)] Thus, normal injection was adopted in the simulation. To evaluate the performance of the scramjet, the 1-D flow model was adopted from the entrance of the inlet to the exit of the internal nozzle and the 2-D flow model was employed for the external nozzle. In the calculation, the air and the combustion gas were ideal gases with constant specific heats. This model is similar to that used in Ref. 8. Procedure of the calculation was as follows:

(1) In no-spillage case, the airflow condition downstream of the shock wave from the leading edge of the airframe was calculated with the 2-D shock wave relations. In the sides-spillage case, the airflow was also affected by the expansion waves from the corners of the leading edge of the airframe (Fig. 1). The mean flow condition to the engine was calculated for each case. The boundary layer on the airframe was ignored in the calculation of the flow condition. The ratio of the specific heats and the molecular weight of air were 1.40 and 28.8, respectively.

(2) There was no spillage from the inlet itself. The flow condition at the exit of the inlet was estimated one-dimensionally with the mass conservation relation, the energy conservation relation and the inlet kinetic energy efficiency. The effect of the inclined airflow during the sides-spillage was included in the kinetic energy efficiency of the inlet. That is, the kinetic energy efficiency of the inlet in the inclined or not-inclined airflow condition would be specified, based on the results of the preliminary inlet tests, which were conducted to investigate the effects of the inclination of the airflow on inlet performance. The apparatus and the results of the tests are described in the following chapters.

(3) Quick, stoichiometric combustion occurred in the constant-cross-section duct one-dimensionally above the flight Mach number of 8. Below Mach 8, the equivalence ratio was adjusted so that the Mach number in the combustor was just above unity to avoid thermal choking. The energy increase at combustion for hydrogen mass flow was 121×10^3 kJ · kg^{-1}. The ratio of the specific heats and the molecular weight of the combustion

gas were 1.25 and 24.7, respectively.

(4) In the internal nozzle, the combustion gas expanded isentropically and one-dimensionally. The cross section at the exit of the internal nozzle was the same as that at the entrance of the inlet. The inviscid thrust at the internal nozzle in the scramjet was evaluated as the difference of the impulse functions at the entrance of the inlet and the exit of the internal nozzle.

(5) At the entrance of the external nozzle, the combustion gas expanded to the nozzle wall surface of 19° isentropically and two-dimensionally (Fig. 1). The inviscid thrust of the external nozzle was the product of the pressure on the wall surface and the projected wall area. The external nozzle was included in the engine here.

(6) A turbulent boundary layer was assumed, and the friction coefficient was set at 0.0025.[11] The friction drag was estimated with the inviscid flow conditions estimated at (1)-(5), and the engine thrust was evaluated by subtracting the friction drag from the sum of the inviscid thrust estimated at (4) and (5).

In the present study, the total thrust was defined as the sum of the engine thrust and the drag on the windward airframe surface. Here, the windward airframe surface consists of the surface from the airframe nose to the engine entrance and the outside surface of the cowl. The drag on the airframe was also affected by the expansion waves of the sides-spillage. In the simulation, the affected area by the sides-spillage was the windward airframe surface (Fig. 1). The affected area spread, e.g., 8.7° from each corner of the airframe leading edge at the flight Mach number of 8, and 6.3° at the Mach number of 12, respectively. The flow condition around the windward surface is examined here under the condition of the flight Mach number of 10. The Mach number behind the shock wave from the leading edge of the airframe is 8 at 6 degrees of the deflection angle between the flight direction and the windward surface. Then the Mach angle behind the shock wave is 7.2 degrees, and the ratio of the pressure increase was 3.7. In this situation, the static pressure matches across the slip line from the leading edge of the airframe with 3 degrees of the slip angle (see Fig. 1). The angle of the shock wave beside the airframe is 8 degrees. The angle is roughly equal to

the Mach angle on the windward surface.

In the flight simulation, the sides-spillage effect was included during the period of scramjet operation. The simulation methods for the flight of the aerospace plane and the airframe data were the same as those used in the previous investigation.[8] The aerospace plane was treated as a material point. The motion of the plane was within the horizontal and vertical plane. The schematic diagram of the forces is shown in Fig. 2, and the equations used in this study are given as follows:

$$\frac{dx}{dt} = \frac{R}{R+z} \cdot u \cdot \cos\gamma \tag{1}$$

$$\frac{dz}{dt} = u \cdot \sin\gamma \tag{2}$$

$$\frac{du}{dt} = \frac{F \cdot \cos\theta - D}{m} - g \cdot \sin\gamma \tag{3}$$

$$\frac{d\gamma}{dt} = \frac{F \cdot \sin\theta + L}{m \cdot u} - \frac{g \cdot \cos\gamma}{u} + \frac{u \cdot \cos\gamma}{R+z} \tag{4}$$

$$\frac{dm}{dt} = -\frac{F}{I_{sp}} \tag{5}$$

From the take-off to the flight Mach number of 6, a hydrogen-fueled air-turbo-ramjet (ATR) propulsion system[12] was used. From Mach 6 to around Mach 12, the scramjet was applied. After the operation of the scramjet engine, the LOX/LH$_2$ rocket engine[13] was used to achieve the low earth orbit at 100 km altitude. The flight dynamic pressure was equal to 100 kPa during the operation of ATR or the scramjet, ex-
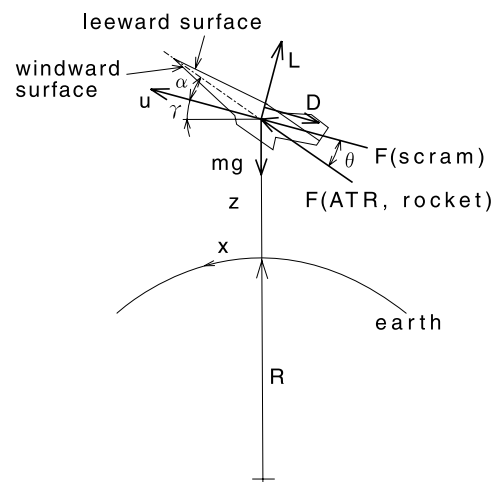

Fig. 2 Force, velocity and coordinates on aerospace plane.

cept at the takeoff.

The initial mass of the aerospace plane was 460 tons at the horizontal take-off. The weight of each part of the aerospace plane, e.g., airframe, engines, was estimated by a weight-analysis program[14] and modification was applied to its results.[8] For example, 51 ton was adopted for the mass of the airframe, whereas the masses of the scramjet, ATR and the rocket engine were 2 %, 6 % and 0.7 % of the initial mass of the aerospace plane, respectively.

Experimental Apparatus

To investigate the effects of the inclination of the airflow due to the sides-spillage on inlet performance, the preliminary test with three inlet models were conducted in a Mach 4 wind tunnel.[1] The inflow total pressure and the total temperature were 2.0 MPa and 290 K, respectively. The cross-section on dimensions of the test section was 10 cm by 10 cm. The Reynolds number was $9 \times 10^7 \mathrm{m}^{-1}$. The thickness of the boundary layer at 99 % of the free stream velocity was 8.7 mm at the entrance of the inlet model.

Figure 3 shows the inlet model, which employed both side-wall compression and ramp compression. The end of the ramp surface coincided with the end of the convergent section of the side-wall. Three ramp configurations were prepared, corresponding to α =0, 5.7°, 8.3°. The heights of the ramps, h_r, were 0 mm, 10 mm, and 15 mm, respectively. The overall contraction ratios of the models were 2, 3, and 4, respectively. Side-wall sweep-back angles were 45°. The shape of

the model was designed for possible variable geometry such that the top-wall could move toward the cowl in the convergent section. The three ramps corresponded to the possible positions of the top-wall. In the present tests, the cowl leading edge was located at the end of the convergent section of the inlet. Downstream of the convergent duct in the inlet was a constant cross-sectional duct, which simulated an isolator.

The entire inlet model was installed on a rotating plate. The plate provided inclination angles of 0, 3°, and 4.5° to the free-stream. The inclination direction was as shown in Fig. 3. In the inclined condition, the right side-wall was on the windward side and the angle to the airflow of the right side-wall increased. At the inclination of 4.5°, the leeward surface of the left side-wall had a negative angle to the free stream.

In the sides-spillage region, the spilled flow inclines parallel to the slip line (Fig. 1). According to the estimation, the angle of the slip line was about 3 degrees in the scramjet operation from the flight Mach number 6 to 12. Therefore, the effect of the inclined flow during the sides-spillage was simulated with the inclination angles of the present tests.

Wall pressure in the model and pitot pressure at the exit of the model were measured by a mechanical pressure scanner with 0.5 seconds per pressure port. Pitot pressure was measured at 45 points in the no-ramp model. The pressures were normalized by the total pressure of the wind tunnel reservoir. The accuracy of the wall pressure and the pitot pressure were ± 0.001 and ± 0.002 in the normalized form, respec-
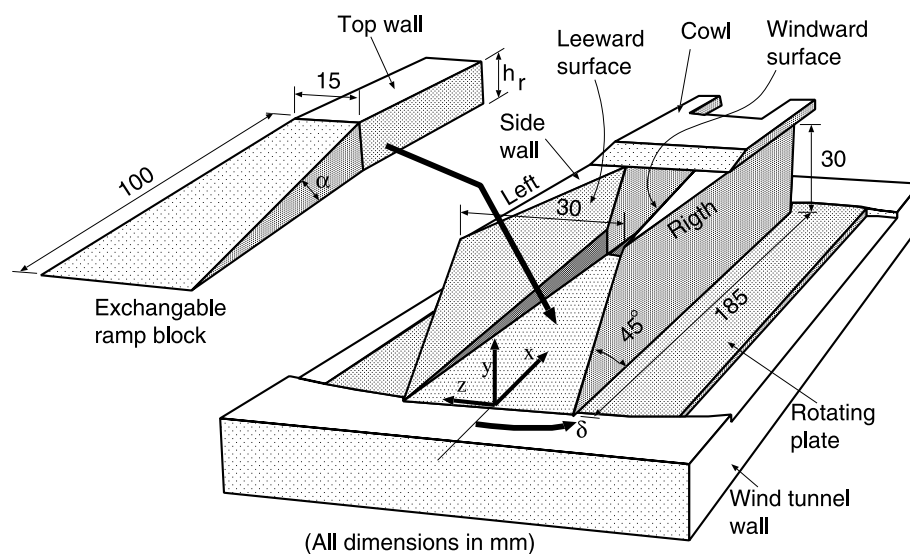

Fig. 3 Inlet model used in the experiments.

Table 1 Estimated upstream airflow conditions

Inclined angle (deg)	Mach No.	Boundary layer thickness (mm)	Mass flow rate to 30×30mm(kg $\cdot$ s^{-1})	Impulse function to 30×30mm(N)	Density (kg $\cdot$ m^{-3})
0	3.95	8.7	0.38	260	0.69
3	3.73	7.0	0.47	320	0.85
4.5	3.63	6.3	0.52	360	0.94

tively. The pitot pressure and the side-wall static pressure at the same height as the pitot tube were used to estimate the total pressure.

The test conditions with the inclination of the model correspond to those of the engine module close to the sides of the airframe, which experiences inclined and expanded airflow. In the evaluation of the inlet performances, the airflow condition upstream of the inclination, i.e., the condition upstream of the supposed expansion waves, should be adopted as a reference condition. The condition was estimated based on the following assumptions.

(1) The inclined angle of the airflow through the supposed expansion waves was identical to the angle of the rotating plate.

(2) The velocity profile in the boundary layer followed the power law, and the profile did not change throughout the expansion.

(3) The mass flow rate in the boundary layer was conserved throughout the expansion.

The upstream Mach number and velocity at the edge of the boundary layer were estimated based on the Prandtl-Meyer function and the assumption (1). The upstream boundary layer thickness was calculated based on the assumptions (2) and (3). The airflow condition upstream of the expansion could be reasonably estimated with the above procedure. In the procedure, the momentum conservation in the boundary layer was ignored. This resulted in an error in the momentum balance of 0.7% when the air was inclined at 4.5°. Table 1 shows the estimated upstream airflow conditions at each inclination.

Experimental Results and Discussion

Oil flow observation

The effect of the inclination of 4.5° on the flow condition in the model is shown in the oil flow patterns of Figs. 4(a), (c) and (e). Figs. 4 (b), (d) and (f) show the patterns with no inclination for comparison. The ramp angles of the model are 0 in (a) and (b), 5.7° in (c) and (d), and 8.6° in (e) and (f), respectively.

In the models with the inclination, a much clearer

(a) No-ramp model at inclination δ = 4.5°
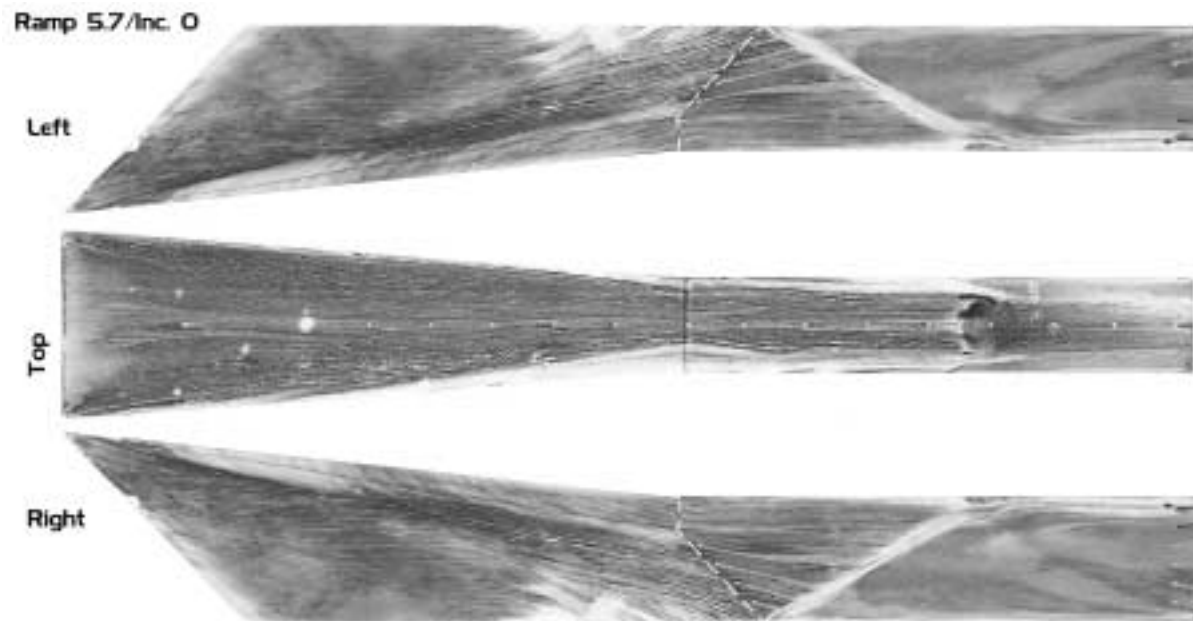
Fig. 4 Oil flow patterns in the inlet models.
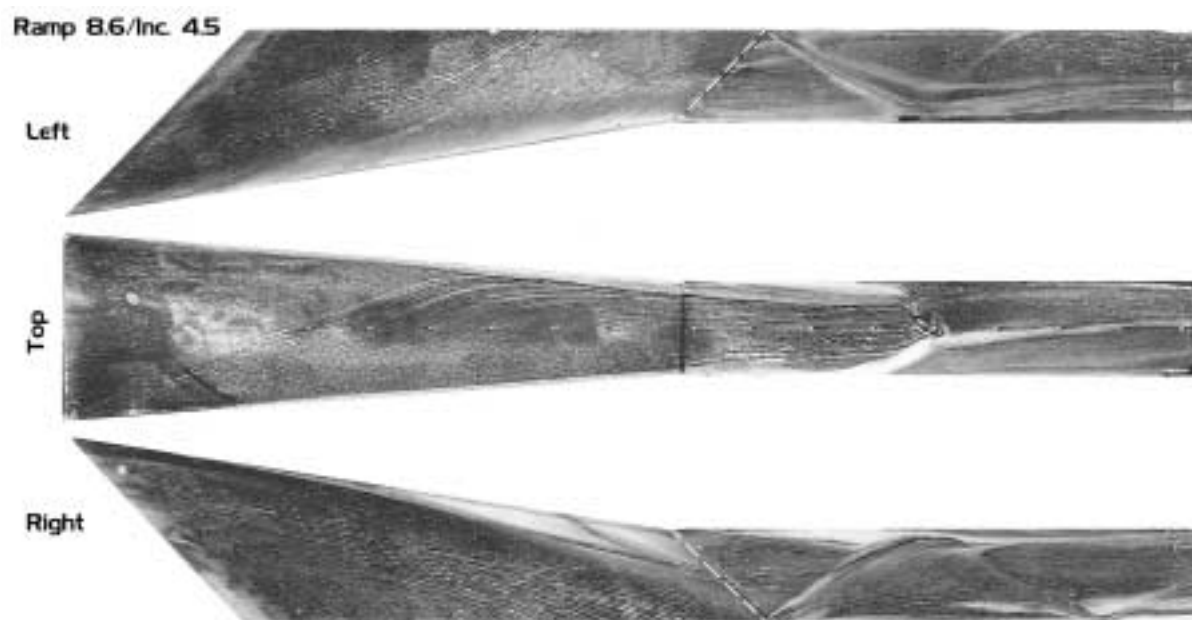
(b) No-ramp model at inclination $\delta = 0°$

(c) Ramp model of $\alpha = 5.7°$ at inclination $\delta = 4.5°$
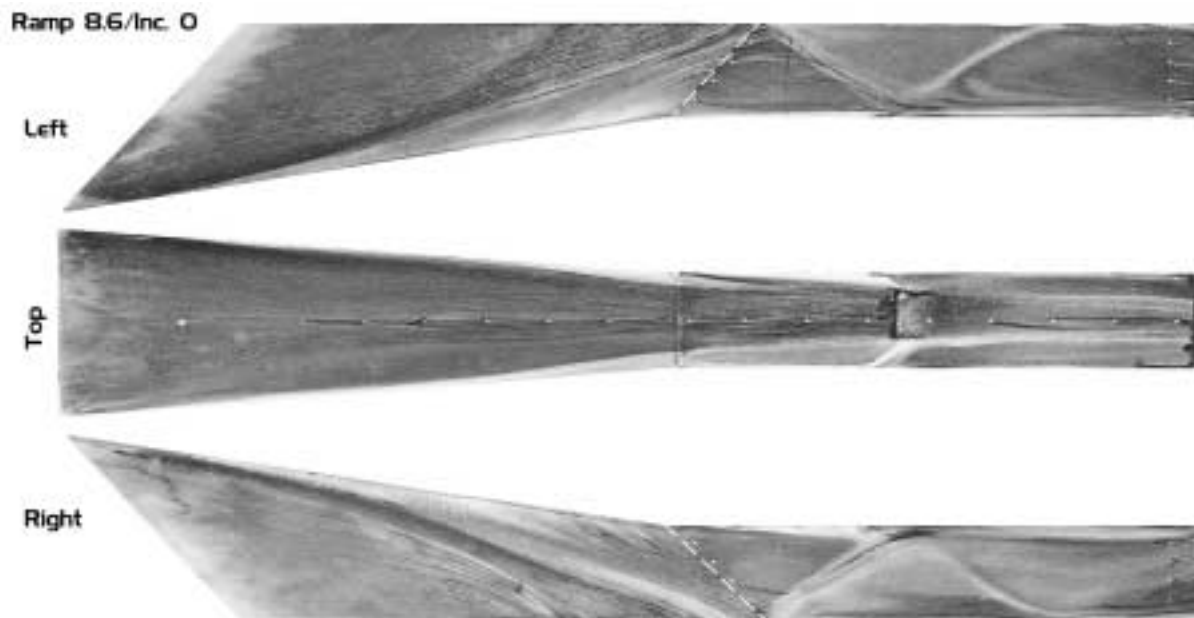
Fig. 4 Oil flow patterns in the inlet models. (cont'd)

Ramp 5.7/Inc. 0

Left

Top

Right

(d) Ramp model of $\alpha = 5.7°$ at inclination $\delta = 0°$

Ramp 8.6/Inc. 4.5

Left

Top

Right

(e) Ramp model of $\alpha = 8.6°$ at inclination $\delta = 4.5°$

Fig. 4 Oil flow patterns in the inlet models. (cont'd)

(f) Ramp model of α = 8.6° at inclination δ = 0°

Fig. 4 Oil flow patterns in the inlet models. (cont'd)

impingement line of the shock wave from the leading edge of the right side-wall on the left side-wall can be seen in the no-ramp model and the 5.7°-ramp model. This indicates the effect of the inclination of the air-flow: the shock wave from the right side-wall was stronger, and the shock wave from the left side-wall was weaker, resulting the difference of the clearness of the line image. In the 8.6°-ramp model, the impingement line could not be distinguished in the inlet section. The effect of the boundary layer was intensified in the ramp model by the spillage of the primary flow.

On the left side of the inlet, deflection of the air-flow toward the cowl was larger than on the right side, and the shock wave from the leading edge of the cowl should therefore be stronger on the left side. However, the cowl shock angle from the horizontal line of 20°, which was estimated from the oil flow pattern, was approximately the same on both sides.

On the top wall, oil flow lines tuned toward the left side-wall in the models with the inclination. Due to the skewness of the shock waves from the cowl, the separation line on the top wall in the isolator was also skewed.

Wall pressure and total pressure distributions

Figures 5 (a) - (c) show the effect of the inclina-tion of the inflow air on the pressure distribution of the top-wall. In Figs. (a) and (b), when the model was inclined, the pressure in the isolator started to increase more upstream due to the shift of the impingement of the cowl shock wave. Though there was observed no shift in the model with the ramp angle of 8.3°, it might be due to the discrete distribution of the pressure ports.

The strengths of the shock waves from the sidewall leading edges and the expansion waves from the throat corner were different on each side due to the inclination of the model. The difference of the shock waves and expansion waves should produce non-uniformity of the pressure locally in the model. However, on the center line of the top-wall, the pressure distribution did not show any large difference. The similarity of the pressure on the top-wall was caused by the thick boundary layer, which obscured the feature. In the low Mach number region, the pressure distribution was mitigated. As the ramp angle increased, the top wall pressure initiated to become large more upstream in the isolator. Because the ramp shock increased with the ramp angle, the angle of the cowl shock wave increased. However, due to the expansion fan from the downstream corner of the ramp, the increased pressure levels in the isolator were almost the

(a) No-ramp model

(b) Ramp model of $\alpha = 5.7°$

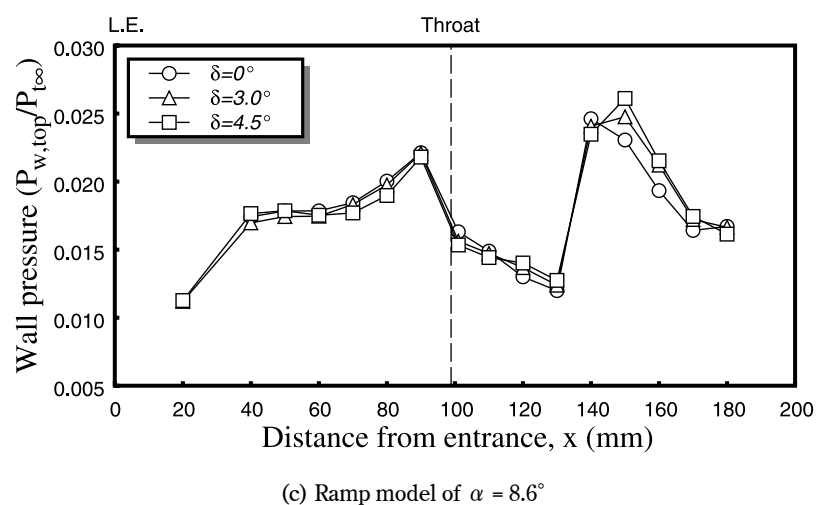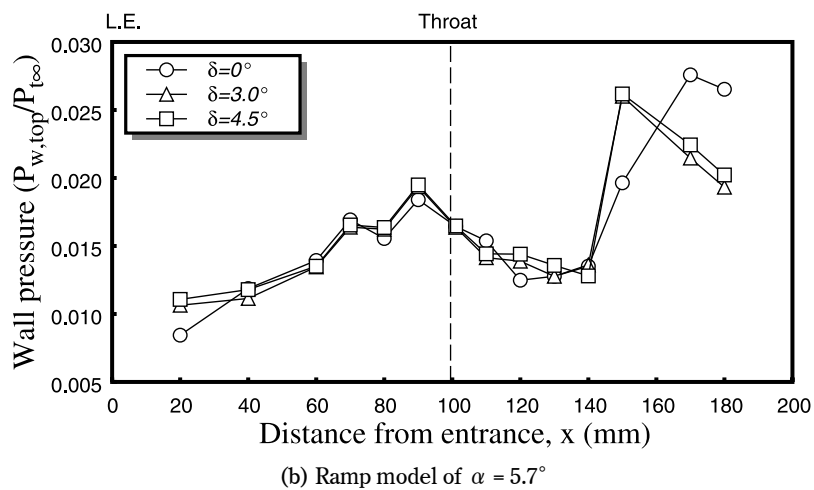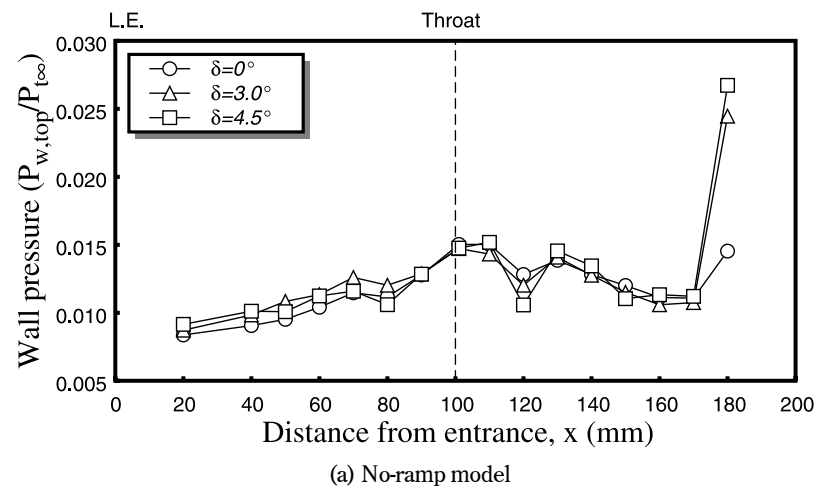
(c) Ramp model of $\alpha = 8.6°$

Fig. 5 Effect of inclination on the top-wall pressure distributions.

same each other.

Figures 6 (a) - (c) show the pressure distribution at the throat of the side-wall. In the figures of the no-ramp model, the top-wall located at y=0 mm, and the cowl at y=30 mm. No significant change of the pressure distribution was observed near the top-wall by the inclination of the model, as was the case on the top-wall. In the no-ramp model, near the cowl, there was no change of pressure level on the right side-wall, i.e., the windward side. However, on the left side-wall, there was a large pressure increase, since the flow on this side went through the stronger shock waves twice, while the flow on the other side did so only once. As the ramp angle increased, the change of the pressure distribution became smaller. The ratio of the affected region by the thick boundary layer to the

channel height became large in the ramp models. The influence of the boundary layer was strengthened by the spillage of the primary flow by the ramp shock wave. However, the effect of the strengthened cowl shock wave by the ramp shock wave did not appear yet at the throat position.

The pressure distributions at the exit of the isolator are shown in Figs. 7(a) - (c). Near the top-wall or near the cowl, there was a shift in pressure level due to the inclination. In the no-ramp model, the shift was observed both near the top wall and near the cowl. Near the top-wall, the impinging point of the cowl shock wave on the top-wall moved upstream with the inclination and the level shifted with the inclination. Furthermore, the difference of the pressure between the right side wall and the left wall increased with the
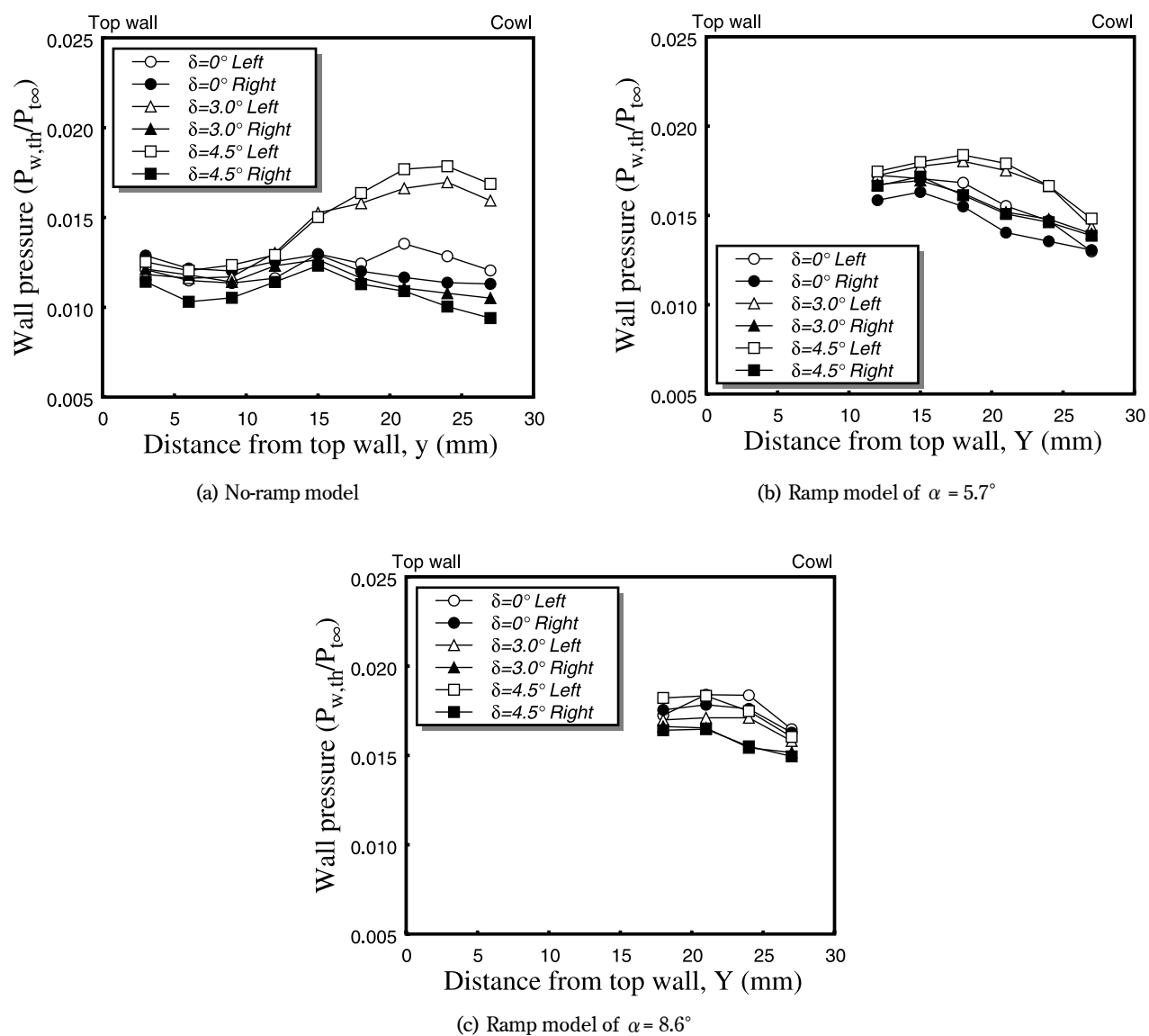

(a) No-ramp model

(b) Ramp model of α = 5.7°

(c) Ramp model of α = 8.6°

Fig. 6 Effect of inclination on the side-wall pressure distributions at the throat of the inlet model.

(a) No-ramp model

(b) Ramp model of $\alpha = 5.7°$
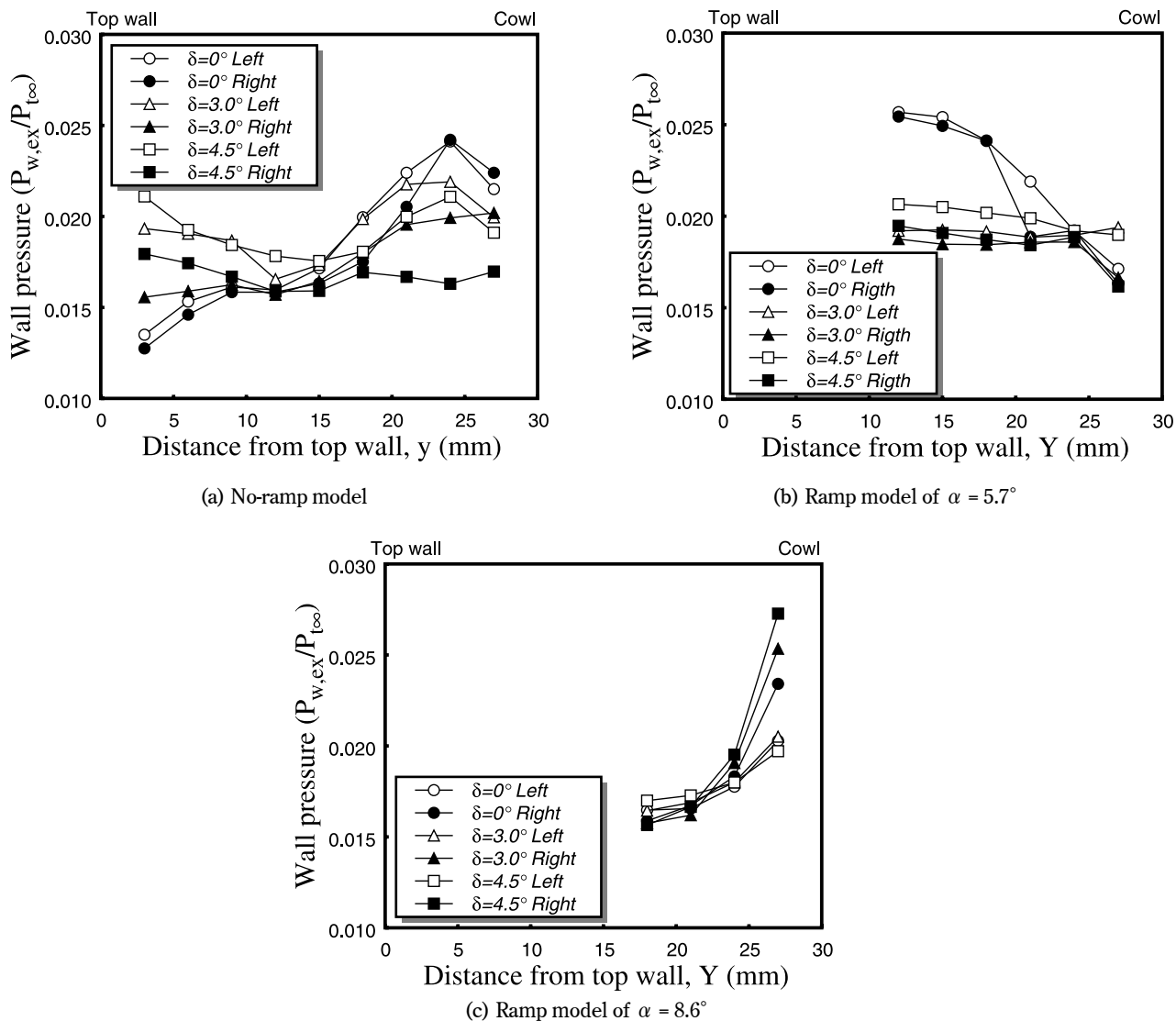
(c) Ramp model of $\alpha = 8.6°$

Fig. 7 Effect of inclination on the side-wall pressure distributions at the exit of the inlet model.

inclination near the top wall or near the cowl. The pressure distribution was skewed with the inclination.

Figures 8(a) - (c) show the total pressure distributions at the exit plane. The right and left side-walls were at z=7.5 mm and -7.5 mm, respectively. In the figure, the cross and the circle represent the positions of the lowest and the highest total pressures, respectively. When there was no inclination, the distribution was approximately symmetrical. Near the top-wall, there was a low total-pressure region, which was caused by the thick boundary layer. The total pressure was high around the center, then decreased near the cowl. With the inclination, in the no-ramp model, the area with high total pressure spread on the right side between the mid and the cowl, and the contour

lines were skewed. In the ramp-models, the symmetry of the distribution decreased with the inclination, as well as in the no-ramp model, and the contour lines became skewed.

Inlet performance

Table 2 lists average Mach numbers, total pressure efficiencies, mass capture ratios, and impulse functions at the exit of the models. In the table, 'mass capture ratio with sides-spillage' and 'impulse function ratio with sides-spillage' used the flow conditions upstream of the supposed expansion listed in Table 1 as the references. The estimation method of the flow condition upstream of the expansion was described in the section 'Experimental apparatus.'
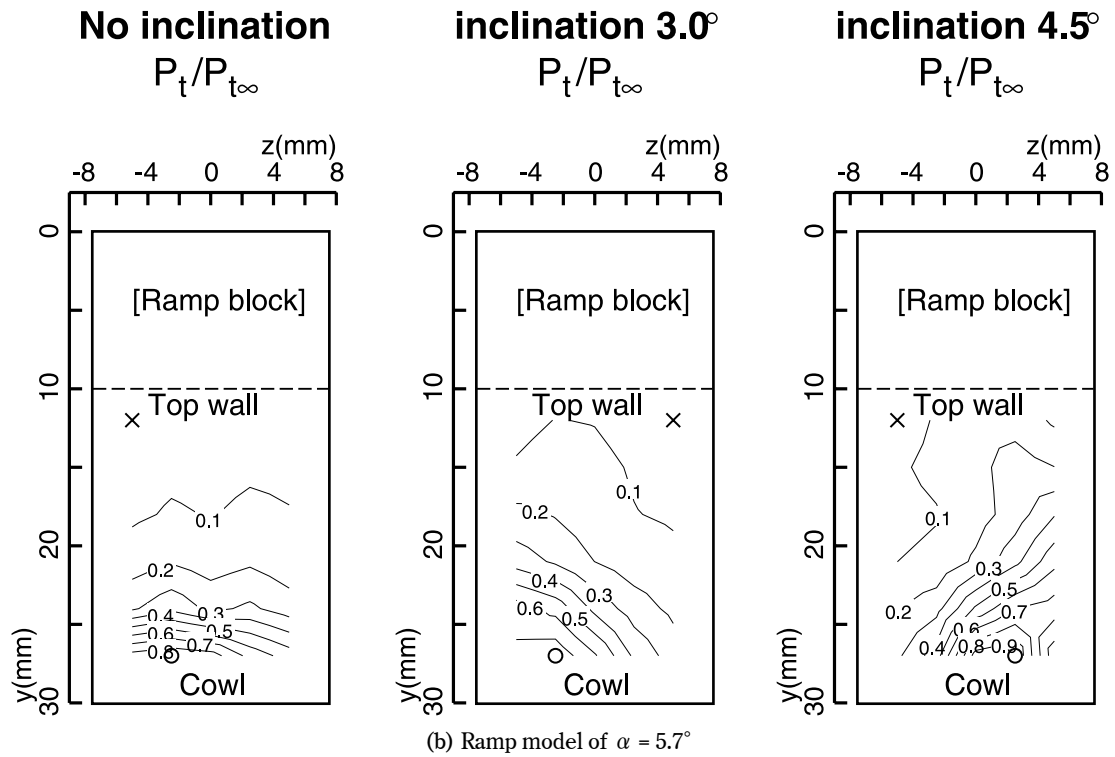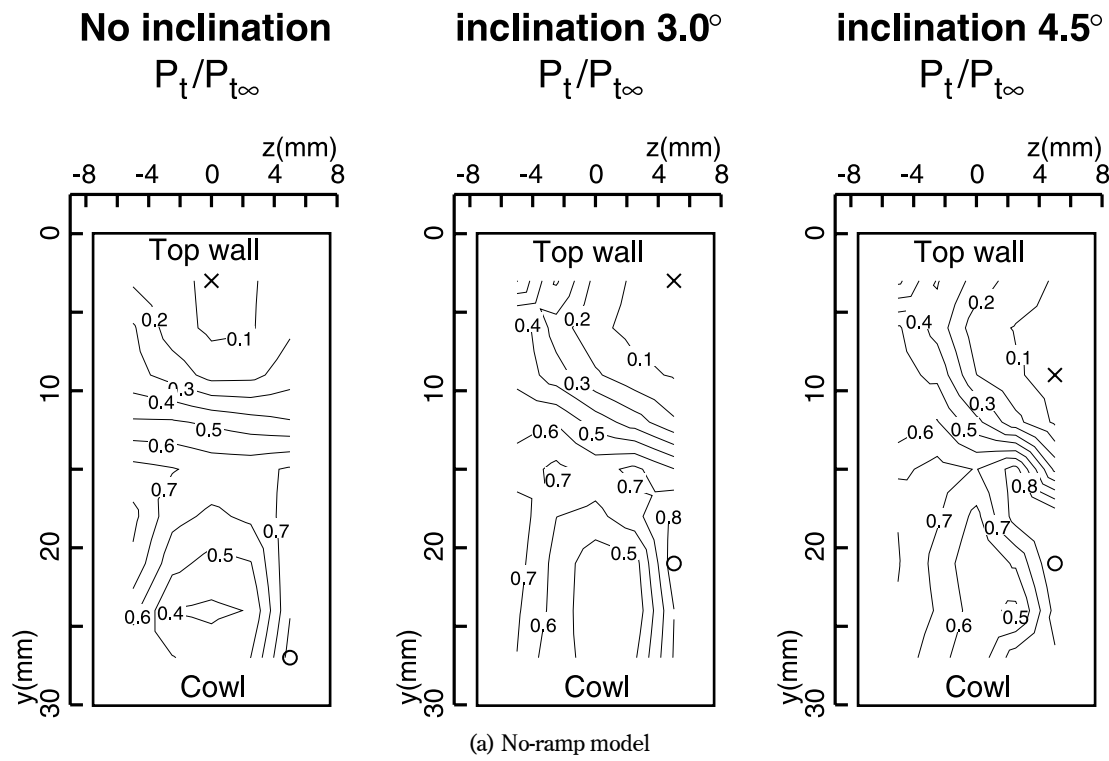
No inclination
$P_t/P_{t\infty}$

inclination 3.0°
$P_t/P_{t\infty}$

inclination 4.5°
$P_t/P_{t\infty}$

(a) No-ramp model

No inclination
$P_t/P_{t\infty}$

inclination 3.0°
$P_t/P_{t\infty}$

inclination 4.5°
$P_t/P_{t\infty}$

(b) Ramp model of $\alpha = 5.7°$

Fig. 8 Effect of inclination on total pressure distributions at the exit of the inlet model.

No inclination
$P_t/P_{t\infty}$

inclination 3.0°
$P_t/P_{t\infty}$

inclination 4.5°
$P_t/P_{t\infty}$
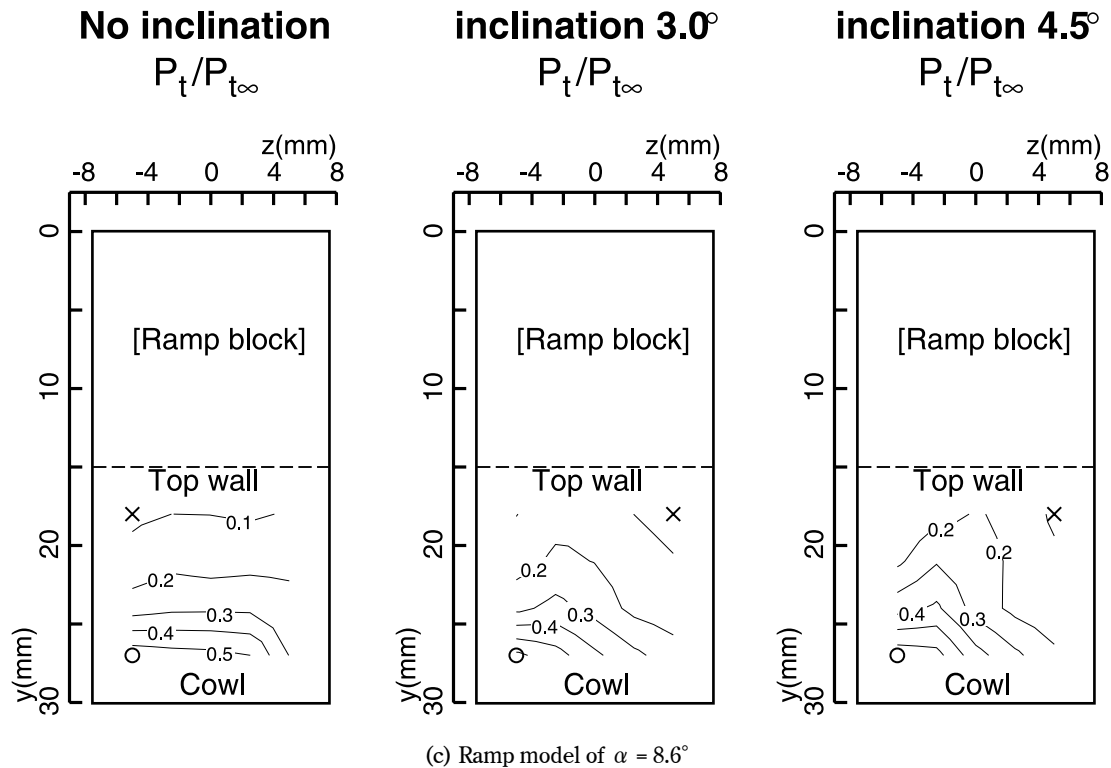

(c) Ramp model of $\alpha = 8.6°$

Fig. 8 Effect of inclination on total pressure distributions at the exit of the inlet model.

Table 2 Inlet model performances

Ramp angle of inlet model	Inclination	Average exit Mach No.	Total pressure efficiency	Mass capture with sides-spillage	Mass capture of inlet	Impulse function with sides-spillage	Impulse function of inlet
0°	0°	2.74	0.53	0.74	0.74	0.627	0.627
	3°	2.75	0.55	0.59	0.74	0.506	0.624
	4.5°	2.81	0.58	0.54	0.75	0.469	0.640
5.7°	0°	2.27	0.37	0.37	0.37	0.278	0.278
	3°	2.36	0.34	0.30	0.38	0.267	0.295
	4.5°	2.47	0.40	0.29	0.41	0.239	0.327
8.6°	0°	2.36	0.32	0.29	0.29	0.233	0.233
	3°	2.31	0.30	0.23	0.29	0.186	0.229
	4.5°	2.37	0.33	0.22	0.31	0.181	0.247

$$(\text{mass capture ratio with sides - spillage}) = \frac{(\text{mass flow rate at the inlet exit})}{(\text{mass flow rate upstream of the supposed expansion})}$$

$$= \frac{\int \rho_2 u_2 dA_2}{\int \rho_0 u_0 dA_1}$$

$$(\text{impulse function ratio with sides - spillage}) = \frac{(\text{impulse function at the inlet exit})}{(\text{impulse function upstream of the supposed expansion})}$$

$$= \frac{\int \left(\rho_2 u_2^2 + P_2\right) dA_2}{\int \left(\rho_0 u_0^2 + P_0\right) dA_1}$$

'Mass capture ratio of inlet' and 'impulse function ratio of inlet' used flow conditions at the entrance of the inlet model as the references. In other words, 'mass capture ratio of inlet' and 'impulse function ratio of inlet' represented the sole performance parameters in the inlet in the inclined flow.

$$\text{(mass capture ratio of - inlet)} = \frac{\text{(mass flow rate at the inlet exit)}}{\text{(mass flow rate at the inlt entrance)}}$$

$$= \frac{\int \rho_2 u_2 dA_2}{\int \rho_1 u_1 dA_1}$$

$$\text{(impulse function ratio of inlet)} = \frac{\text{(impulse function at the inlet exit)}}{\text{(impulse function at the inlt entrance)}}$$

$$= \frac{\int \left(\rho_2 u_2{}^2 + P_2\right) dA_2}{\int \left(\rho_1 u_1{}^2 + P_1\right) dA_1}$$

With inclination to the airflow, the total pressure efficiency and the Mach number increased. However, the changes due to the inclination were small. The measured total pressure efficiency corresponded to a kinetic energy efficiency of 0.95 in the no-ramp model. 'Mass capture ratio of inlet' did not change significantly by the inclination, i.e., the inclination of the airflow to the inlet did not change the inlet spillage significantly. 'Impulse function ratio of inlet' did not change significantly by the inclination, either. This means that the stream thrust function was approximately the same in each ramp model. Though the airflow remained skewed, the average performance of the inlet did not change significantly due to the inclination of the incoming airflow.

'Mass capture ratio with sides-spillage' decreased with the inclination. Because the density decreased significantly through the supposed expansion waves, the estimated mass flow rate upstream of the expansion waves became larger with inclination as listed in Table 1. Beside the sides-spillage, the mass flow rate at the throat of the inlet is reduced by spillage from the open bottom of the inlet, and this spillage changes due to the Mach number and the shock wave structure in the model. In the current experiment, the change of the entrance Mach number due to the inclination was, at most, 0.3, as listed in Table 1. According to the calculated results using the 2-D shock wave relations, [15] a shift of the entrance Mach number of 0.3 for Mach 4 would cause the change of the mass capture ratio by up to 5%. The changes in the mass capture ratio with expansion listed in Table 2 were much larger than 5%, indicating that the decrease of the mass capture ratio was primarily caused by the decrease of the density throughout the expansion. 'Impulse function ratio with sides-spillage' also decreased

primarily due to the decrease of the mass capture ratio. This means that the spilled impulse function increases due to the sides-spillage upstream of the inlet, and thus the engine thrust decreases.

In the model with the ramp top-wall, the total pressure and the impulse function are small, because of the spillage of the primary flow by the ramp shock wave. The cowl should be extended forward to prevent spillage. The effect of the cowl extension is described in Appendix.

Simulation Results and Discussion

The experiments proved that the sides-spillage decreased the mass flow rate into the inlet significantly, but did not affect the aerodynamic performance of the inlet significantly. In the simulation, only the airflow to the engine was reduced by the sides-spillage. The assumption of the constant kinetic energy efficiency of the inlet regardless of the sides-spillage was reasonable in the following simulation. The kinetic energy efficiency of inlets is nearly constant with flight Mach number.[16] The kinetic energy efficiency of the inlet was set to be 0.98, which was attained by the empirical equation.[17] Approximately the same value of the inlet was attained in the tests with the sub-scale scramjet model.[9],[10] The low efficiency in the present experiments of 0.95 was due to the thick boundary layer.

Engine performance

Figure 9 shows the thrust coefficients of the engine models. The coefficient is defined as the ratio of the total thrust to the product of the flight dynamic pressure and the projected cross section of the engine at the entrance. The results with 'side fence' and 'side ramp' will be mentioned later. Figure 10 shows the mass flow rate into the engine, which is non-
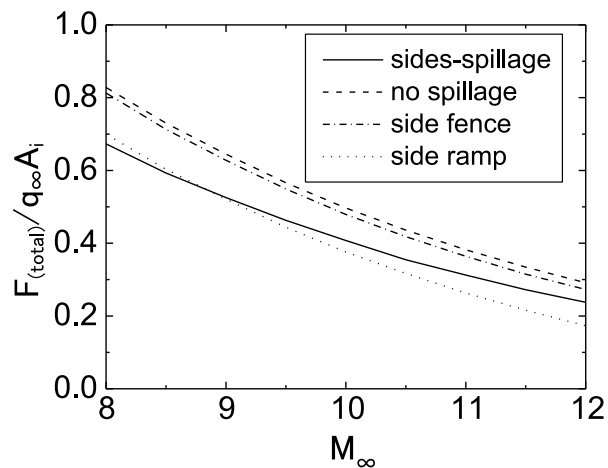
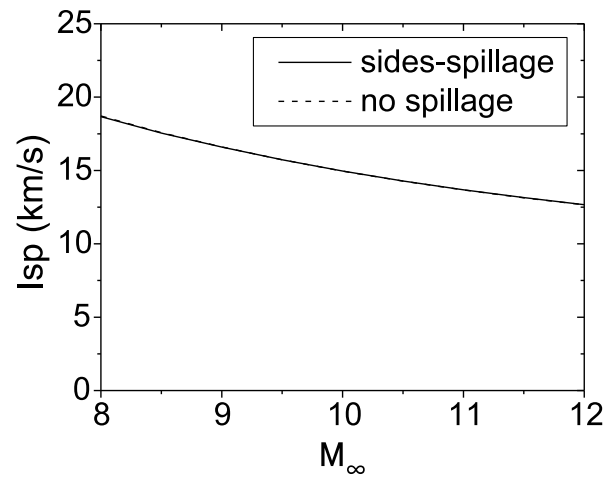Fig. 9 Effect of the sides-spillage on thrust coefficient.

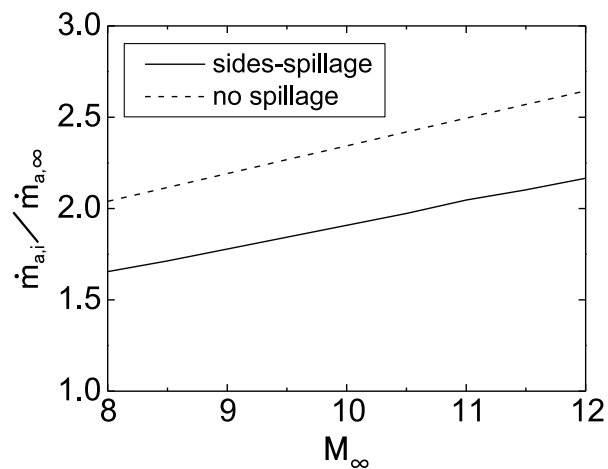Fig. 11 Effect of the sides-spillage on the specific impulse.

Fig. 10 Effect of the sides-spillage on the air mass flow rate into the scramjet engine.

Fig. 12 Thrust/drag contents of the aerospace plane at a flight Mach number of 10.

dimensionalized by the product of the mass flux of the free stream and the projected cross section of the engine at the entrance. Figure 11 shows the specific impulses of the engine models.

The thrust coefficient of the engine with the sides-spillage was 15% lower than that of the engine with no spillage. This was caused by the smaller mass flow rate into the engine, as shown in Fig. 10. There was only slight difference in the specific impulse between the models, thus the specific impulse did not contribute the decrease of the thrust coefficient. The total enthalpy of the inflow air and the contribution of heat addition due to combustion were the same in the models at each flight Mach number, so the specific impulse did not change significantly. The small discrepancy between the trends in thrust coefficients and mass flow rates was caused by the difference in pressure on the windward airframe surface. Figure 12
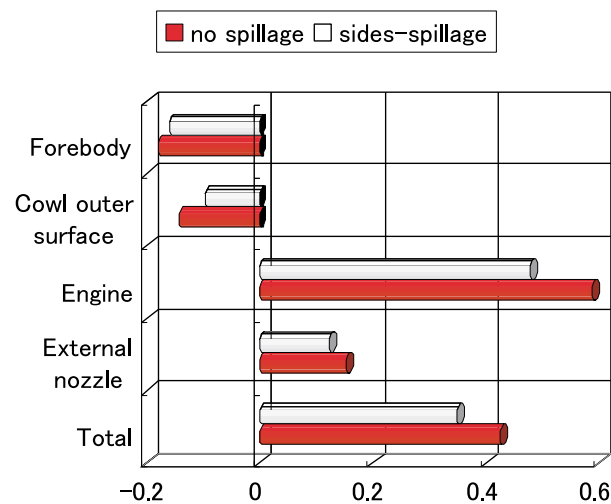
shows the breakdown of thrust/drag at a flight Mach number of 10. The effect of the sides-spillage slightly decreased the pressure drag of the aerospace plane. However, the decline in the engine-produced thrust was much larger than the decrease in drag on the airframe.

To prevent sides-spillage, side-fences and side-ramps, as shown in Fig. 13, are options. The total thrust with each option was calculated to clarify its effectiveness. The fences were attached to the sides of the airframe from the nose of the airframe to the entrance of the engine. No propagation of the expansion waves from the sides of the airframe was assumed. The thickness of the fences and the pressure drag on them were neglected. The friction drag on the fences was counted in the total thrust.
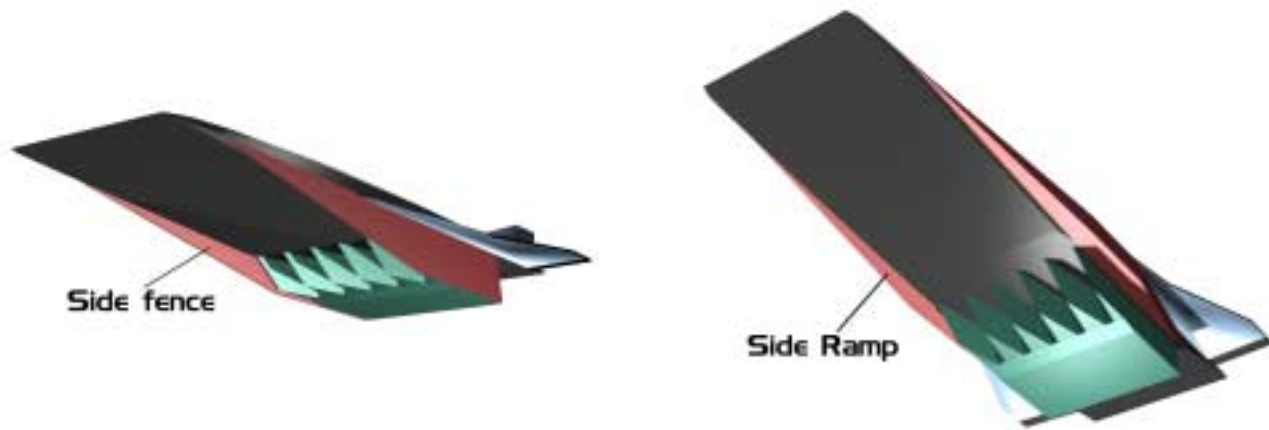
Fig. 13 Schematic diagrams of (a) an aerospace plane with side-fences and (b) a plane with side-ramps.

The side surfaces of the body for the model with the side-ramps had an angle of 6° from the flight direction. This angle was chosen to be the same as the sum of the windward airframe angle and the angle of attack. With this configuration, the pressure on the windward surface was expected to be approximately the same as that on the surface of the side-ramps, which means that there was no formation of expansion waves to the windward surface from the sides of the airframe, and no spillage. The effects of the pressure on the leeward side of the airframe and of the formation of the secondary flow on the pressure on the side-ramps were neglected. The pressure drag on the ramp surfaces was included in the total thrust.

The resulting engine performances are also shown in Fig. 9. The friction drag on the fences decreased the thrust slightly from that of the model with no sides-spillage, and the result showed the fences to be effective for suppression of the decrease in thrust due to the sides-spillage. When the fences are attached to the airframe, additional secondary flows may appear, e.g., vortex flow at the corner of the airframe and the fences. This may cause engine-starting problems. By making the gap between the inlet and the side fence, the vortex flow at the corner will be evacuated outside the engine. The side-ramps increased pressure drag and the thrust was lower than that with the sides-spillage. The attachment of the side-ramps was a negative factor for thrust.

Payload estimation

An additional drag or weight penalty due to employment of modification devices, e.g., side-fences or side-ramps, was not included in the flight simulation.

In the present study, the scramjet operated up to a flight Mach number of 11 in both the sides-spillage and the no-spillage conditions. When the scramjet was used up to Mach 11, the payload became maximum in both conditions. Figure 14 shows the flight conditions of the sides-spillage case and the no-spillage case. Table 3 lists the contents of the mass ratios of the aerospace plane.

The effect of the sides-spillage was included during the scramjet operation in this study. The operating time was longer with the sides-spillage case because of the low thrust. In addition, the fuel consumed during the scramjet operation was increased by 6.5 tons with the sides-spillage. Finally, the payload for the scramjet vehicle with the sides-spillage was 3.9 tons, while that with no-spillage was 6.9 tons. Hence, the payload was 43 % lower than that with no-spillage.
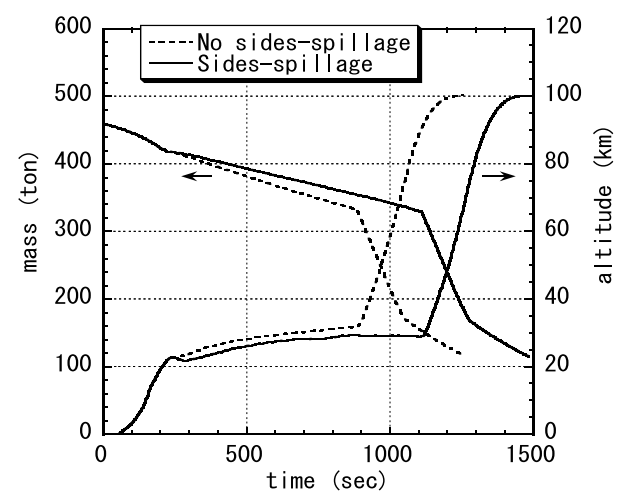

Fig. 14 Flight conditions of the sides-spillage case and no-spillage case.

Table 3 Contents of mass ratio in aerospace plane.

	Fuel	Oxidizer	Fuel tank	Oxidizer tank	Airframe	Engines	Payload
No spillage	0.295	0.451	0.033	0.008	0.111	0.087	0.015
With sides-spillage	0.308	0.443	0.035	0.007	0.111	0.087	0.008

Assuming the aerospace plane went into an orbit of 200 km, the payloads of both operations were 2.0 tons with the sides-spillage and 4.9 tons with no-spillage. The payload level became smaller at the higher orbit, and the ratio of the payloads further decreased due to the sides-spillage. Each part of the aerospace plane may become heavier than the predicted value. Then the payload of each mission will become smaller, and the ratio of the payloads further decreased due to the sides-spillage.

If light-weight side-fences under 3 tons could be manufactured, prevention of sides-spillage would be beneficial. The volume of a side-fence was about 0.3 m^3, assuming a thickness of 1 cm. If nickel-alloy panel-structure with 1 mm average-thickness and ceramic tile are used for the fences, the weights of the structure and the tile become 530 kg and 100 kg, respectively. The weight of the fences becomes 630 kg, and the actual weight will be around the present estimation. Attachment of the fences is advantageous.

Concluding remarks

The authors investigated the effects of the sides-spillage, i.e., the spillage of the airflow by propagation of expansion waves from the sides of the airframe, on the performance of the scramjet and the aerospace plane. The effect on the inlet performances by the sides-spillage was preliminary investigated in Mach 4 wind tunnel, and the primary features of the sides-spillage were attained. Then numerical simulations of the scramjet engine and the flight of the aerospace plane were conducted. The investigations clarified the following points.

(1) The inclination of the incoming airflow by the sides-spillage had only small effect on the average performance of the inlet models.

(2) The major effect of the sides-spillage was the decrease of the mass capture ratio.

(3) The thrust decreased by 15 % due to the sides-spillage caused by the decrease of the airflow rate, and the payload also decreased to 60 % due to the sides-spillage.

(4) Side-fences were beneficial to prevent the sides-spillage. The attachment of the side-ramps was a negative factor for thrust.

Acknowledgements

References

(1) Huebner, L. D.; Computational Inlet-Fairing Effects and Plume Characterization on a Hypersonic Powered Model, Journal of Aircraft, Vol. 32, No. 6 (1995) pp. 1240 - 1245.

(2) Hozumi, K., Watanabe, S., Nomura, S.; Aerodynamic Studies on Space Plane Configuration at Hypersonic Speed, Proceedings of the 17th International Symposium on Space Technology and Space Science, International Symposium on Space Technology and Space Science Committee, Tokyo, Japan (1990/5) pp. 1365 - 1376.

(3) Weinreich, H.-L., Grallert, H., Parkinson, R., and Berry, W.; Studies of a Scramjet-propelled, Horizontal Launch and Landing, Single-Stage-to-Orbit Launcher, AIAA Paper 93-5053 (1993/11).

(4) Lockwood, M. K., Hunt, J. L., Kabis, H., Moses, P., Pao, J.-L., Yarrington, P., and Collier, C.; Design and Analysis of a Two-Stage-to-Orbit Airbreathing Hypersonic Vehicle Concept, AIAA Paper 96-2890 (1996/7).

(5) Kanda, T., Komuro, T., Masuya, G., Kudo, K., Murakami, A., Tani, K., Wakamatsu, Y., and Chinzei, N.; Mach 4 Testing of Scramjet Inlet Models, Journal of Propulsion Power, Vol. 7, No. 2 (1991) pp. 275-280.

(6) Tani, K., Kanda, T., Kudou, K., Murakami, A., Komuro, T., and Ito. K.; Aerodynamic Performance of Scramjet Inlet Models with a Single Strut, AIAA Paper 93-0741, (1993/1).

(7) Tani, K., Kanda, T., Tokunaga, T.; Starting Characteristics of Scramjet Inlets, Proceedings of 11th International Symposium on Air Breathing Engines, AIAA, Washington, DC (1993/9) pp. 1071-1080.

(8) Kanda, T., and Kudo, K.; Payload to Low Earth Orbit by Aerospace Plane with Scramjet Engine, Journal of Propulsion Power, Vol. 13, No. 1 (1997) pp. 164-166.

(9) Kanda, T., Hiraiwa, T., Mitani, T., Tomioka, S., and Chinzei, N.; Mach 6 Testing of a Scramjet Engine Model, Journal of Propulsion and Power, Vol. 13, No. 4 (1997) pp. 543 - 551.

(10) Kanda, T., Wakamatsu, Y., Ono, F., Kudo, K., Murakami, A., and Izumikawa, M.; Mach 8 Testing of a Scramjet Engine Model, AIAA Paper 99-0617 (1999/1).

(11) Swithenbank, J.; Hypersonic Airbeathing Propulsion, Progress in Aeronautical Sciences, Vol. 8, Pergamon Press, Oxford, U. K., 1st ed. (1967) p. 245.

(12) Sakata, K., Yanagi, R., Shindo, S., Minoda, M., and Nouse, H.; Conceptual Study on Air-Breathing Propulsion for Space Plane, Proceedings of 16th International Symposium on Space Technology and Science, Committee of International Symposium on Space Technology and Science, Tokyo, Japan (1988/5) pp. 107-112.

(13) Kanmuri, A., Kanda, T., Wakamatsu, Y., Torii, Y., Kagawa, E., and Hasegawa, K.; Transient Analysis of LOX/LH2 Rocket Engine (LE-7), AIAA Paper 89-2736 (1989/7).

(14) Glatt, C. R.; WAATS - A Computer Program for Weight Analysis of Advanced Transportation Systems, NASA CR-2420 (1974/9).

(15) Trexler, C. A., and Souders, S. W.; Design and Performance at a Local Mach Number of 6 of an Inlet for an Integrated Scramjet Concept, NASA TN D-7944 (1975/8).

(16) Kerrebrock, J. L.; Some Readily Quantifiable Aspects of Scramjet Engine performance, Journal of Propulsion and Power, Vol. 8, No. 5 (1992) pp. 1116-1122.

(17) Heiser, W. H., Pratt, D. T., Daley, D. H., and Mehta, U. B.; Hypersonic Airbreathing Propulsion, edited by J. S. Przemieniecki, AIAA Education Series (1994) p. 225, AIAA, Washington, DC.

Appendix

In order to investigate the effect of the cowl extension on reduction of spillage, the cowl leading edge was extended 20 mm upstream from the end of the convergent section in the model of the ramp angle α =5.7° with no inclination. The model with the extended cowl is designated as 'the extended-cowl model," whereas the model with no cowl extension

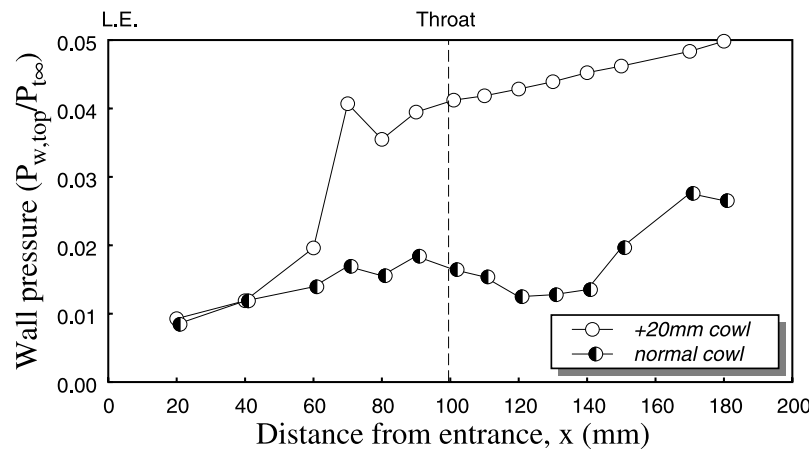Fig. A-1 Oil flow pattern of the extended-cowl model (ramp model α = 5.7° , inclination δ =0°).

Fig. A-2 Effect of the extension of the cowl on the top-wall pressure distribution.
(ramp model $\alpha = 5.7°$ at inclination $\delta = 0°$).

and the same ramp configuration as 'normal-cowl model.'

Figure A-1 shows the oil flow patterns in the cowl-extended model. There was no pattern of separation on the ramp surface of the top wall, suggesting that the inlet was in the start condition.

Figure A-2 shows the pressure distribution on the top wall. The pressure at the entrance of the ramp agreed with that of the no-extended-cowl model. The top wall pressure became larger than that of the normal cowl model on the ramp surface. There was no impingement of a shock wave around x=60mm, thus the inlet was in the partially-start condition.[A-1] Though there was no trace of separation on the ramp,

the separation region due to the pressure increase in the isolator probably went around the crossing position of the shock waves from the leading edges of the side walls. The pressure level in the isolator was higher than those of the normal cowl model.

Figure A-3 shows the pressure distribution at the throat of the side-wall. In the model, the spillage of the primary flow was reduced and the influence of the boundary layer was weakened. On the left side-wall, there was a large pressure increase, whereas there was small change of pressure level on the right side-wall. Figure A-4 shows the pressure distributions at the exit of the isolator. The uniformity of the pressure distribution was better than at the throat and than that
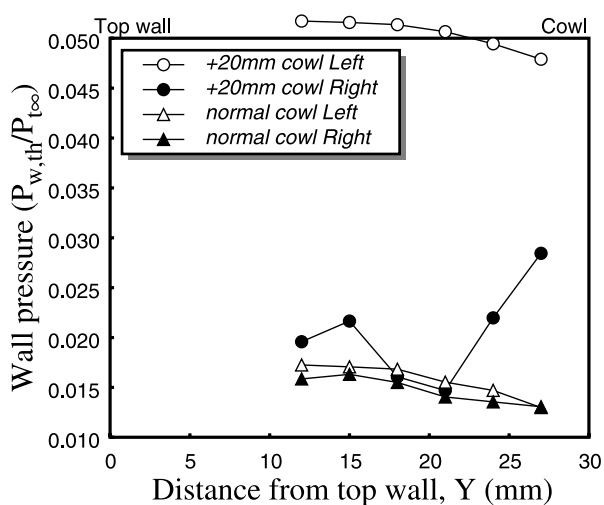

Fig. A-3 Effect of the extension of the cowl on the side-wall pressure distributions at the throat of the model (ramp model $\alpha = 5.7°$, inclination $\delta = 0°$).
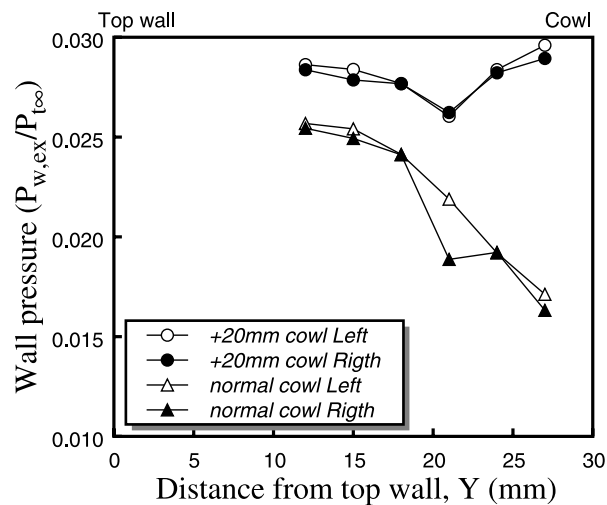

Fig. A-4 Effect of the extension of the cowl on the side-wall pressure distributions at the exit of the model (ramp model $\alpha = 5.7°$, inclination $\delta = 0°$).

Table A-1 Extended-cowl model performance

Inlet model type	Ramp angle of inlet model	Inclination	Average exit Mach No.	Total pressure efficiency	Mass capture of inlet	Impulse function of inlet
Extended-cowl model	5.7°	0°	2.33	0.47	0.56	0.445
Normal-cowl model	5.7°	0°	2.27	0.37	0.37	0.278

of the normal cowl model.

When the cowl was extended upstream, the symmetry of the total pressure distribution was conserved as shown in Fig. A-5. In comparison with the distribution of the normal cowl model in Fig. 8(b), the uniformity of the distribution increased, and, for example, the area with 50% of the total pressure spread to the mid of the channel. As for the performance, the spillage of the primary flow was reduced, and as listed in Table A-1, the mass capture ratio and other properties were improved. The variable geometry inlet with the top-wall moving ramp should be designed in the extended-cowl configuration.

Reference of Appendix

(A-1) Tani, K., Kanda, T., Tokunaga, T.; Starting Characteristics of Scramjet Inlets, Proceedings of 11th Inetrnational Symposium on Air Breathing Engines, AIAA, Washington, DC (1993/9) pp.1071-1080.
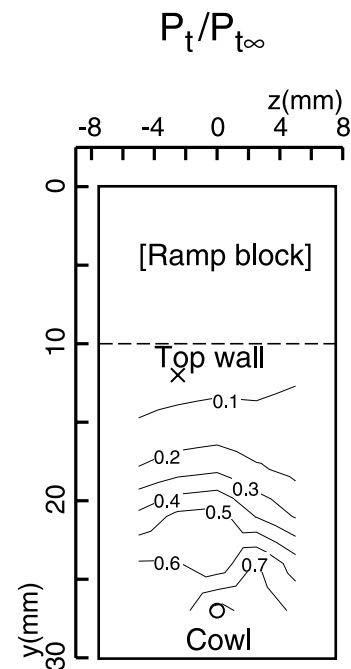
No inclination : cowl +20mm

$P_t/P_{t\infty}$

Fig. A-5 Effect of the extension of the cowl on total pressure distributions at the exit of the model (ramp model $\alpha = 5.7°$, inclination $\delta = 0°$).